



Scale-invariant structures of spiral waves

Daniel Sohn^a, Konstantinos Aronis^a, Hiroshi Ashikaga^{a,b,*}

^a Cardiac Arrhythmia Service, Johns Hopkins University School of Medicine, 600 N Wolfe Street, Carnegie 568, Baltimore, MD, USA

^b IHU Liryc, Electrophysiology and Heart Modeling Institute, Fondation Bordeaux Université, F-33600, Pessac-Bordeaux, France



ARTICLE INFO

Keywords:

information theory
Renormalization
Pattern formation
Coherent structures
Fibrillation
Spiral waves

ABSTRACT

Background: Spiral waves are considered to be one of the potential mechanisms that maintain complex arrhythmias such as atrial and ventricular fibrillation. The aim of the present study was to quantify the complex dynamics of spiral waves as the organizing manifolds of information flow at multiple scales.

Method: We simulated spiral waves using a numerical model of cardiac excitation in a two-dimensional (2-D) lattice. We created a renormalization group by coarse graining and re-scaling the original time series in multiple spatiotemporal scales, and quantified the Lagrangian coherent structures (LCS) of the information flow underlying the spiral waves. To quantify the scale-invariant structures, we compared the value of the finite-time Lyapunov exponent between the corresponding components of the 2-D lattice in each spatiotemporal scale of the renormalization group with that of the original scale.

Results: Both the repelling and the attracting LCS changed across the different spatial and temporal scales of the renormalization group. However, despite the change across the scales, some LCS were scale-invariant. The patterns of those scale-invariant structures were not obvious from the trajectory of the spiral waves based on voltage mapping of the lattice.

Conclusions: Some Lagrangian coherent structures of information flow underlying spiral waves are preserved across multiple spatiotemporal scales.

1. Introduction

Spiral waves are one of the potential mechanisms that maintain complex arrhythmias such as atrial and ventricular fibrillation in humans [1]. The outcomes of interventional catheter ablation therapy targeting rotors, the rotational centers of spiral waves, for treatment of atrial fibrillation have been conflicting [2–6]. Those conflicting results from clinical studies suggest that our current understanding of the mechanism of fibrillation is far from complete.

Spiral waves are an emergent macroscopic collective behavior of the heart resulting from interactions among a large number of cells at the microscopic scale. We recently developed an information-theoretic approach to numerically quantify the complex interactions occurring at the microscopic scale as the organizing manifolds of information flow [7]. Those manifolds, called Lagrangian coherent structures (LCS) [8–10], include two types: (1) Repelling LCS quantify stretching along a material line, and indicate walls through which the flow does not traverse, and (2) attracting LCS quantify folding along a material line, and indicate channels through which flow is funneled. Some repelling and attracting LCS of rotors become more clearly defined over a longer

observational period. This finding suggests that the LCS that is relatively stable over time contributes to maintenance of spiral waves. In addition, our recent work demonstrated that the mechanism that maintains spiral waves can be quantified as information flow from macro-to micro-scale behaviors of the cardiac system [11]. Taken together, these findings suggest that the mechanism that maintains spiral waves can be quantified as the scale-invariant LCS.

The aim of the study was to quantify the complex interactions occurring during spiral wave reentry at multiple scales. Specifically, we aimed to quantify structures beyond phase singularities of spiral waves. To accomplish this aim, we applied iterated coarse-graining and re-scaling [12] to the microscopic description of the cardiac system with spiral waves to generate a renormalization group in a series of spatiotemporal scales [11,13]. We hypothesized that the LCS of information flow underlying spiral waves are scale-invariant.

2. Methods

We performed the simulation and the data analysis using Matlab R2017a (Mathworks, Inc.).

* Corresponding author. Cardiac Arrhythmia Service, Johns Hopkins University School of Medicine, 600 N Wolfe Street, Carnegie 568, Baltimore, MD, USA.

E-mail address: hashika1@jhmi.edu (H. Ashikaga).

URL: <https://www.hiroshiashikaga.org/> (H. Ashikaga).

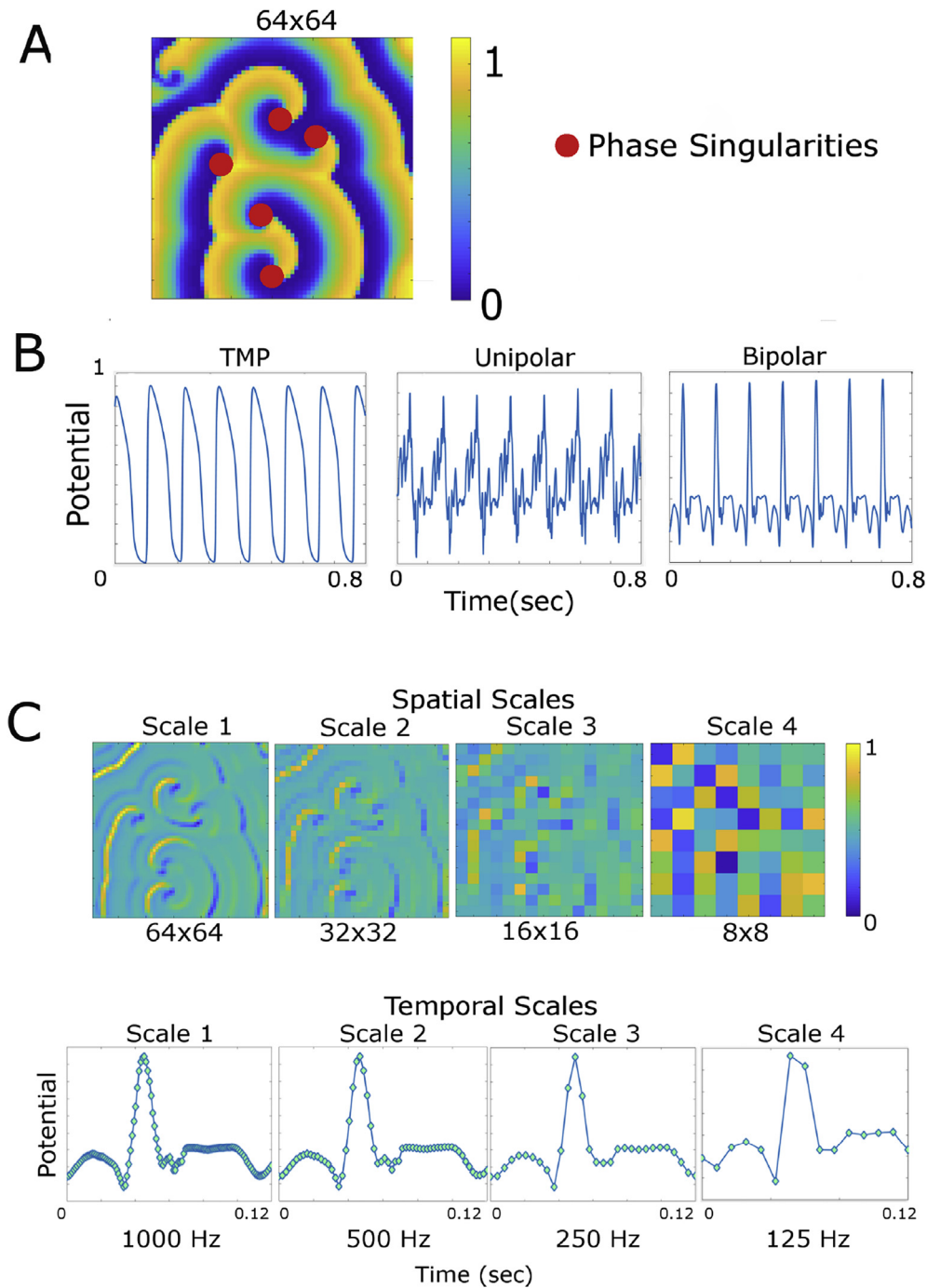


Fig. 1. Conceptual overview. *A. Spiral waves and rotors.* Spiral waves in a 64×64 lattice. The transmembrane potential is color-coded (arbitrary unit between 0 and 1). The rotors are defined as the phase singularities of the phase map (filled red circles). *B. Conversion to bipolar electrogram.* The transmembrane potential (TMP, left panel) derived from the model was converted to unipolar (middle panel) and subsequently to bipolar electrogram (right panel). *C. Renormalization group.* The bipolar electrogram is color-coded (arbitrary unit between 0 and 1). Spatial scales include scale 1 (64×64 lattice), scale 2 (32×32 lattice), scale 3 (16×16 lattice), and scale 4 (8×8 lattice). Temporal scales include scale 1 (1000 Hz), scale 2 (500 Hz), scale 3 (250 Hz), and scale 4 (125 Hz). Each circle represents a data sampling point. (For interpretation of the references to color in this figure legend, the reader is referred to the Web version of this article.)

2.1. Model of spiral waves

We used a deterministic, phenomenological model of the cardiac action potential described by Fenton and Karma [14]. This model accurately reproduces action potential duration (APD) restitution, APD alternans, conduction block, and spiral wave initiation, which are important properties of cardiac action potential [15]. The model consists of three variables: the transmembrane potential V , a fast ionic gate u , and a slow ionic gate w .

$$\frac{\partial V}{\partial t} = D \left(\frac{\partial^2 V}{\partial x^2} + \frac{\partial^2 V}{\partial y^2} \right) - \frac{I_{fi} + I_{so} + I_{si} + I_{ext}}{C_m} \quad (1)$$

Here C_m is the membrane capacitance ($= 1 \mu F/cm^2$) and D is the diffusivity with value $0.001 \text{ cm}^2/\text{ms}$ to represent a two-dimensional (2-D) isotropic system [15]. The current I_{fi} is a fast inward inactivation current used to depolarize the membrane when an excitation above threshold is induced. The current I_{so} is a slow, time-independent rectifying outward current used to repolarize the membrane back to the

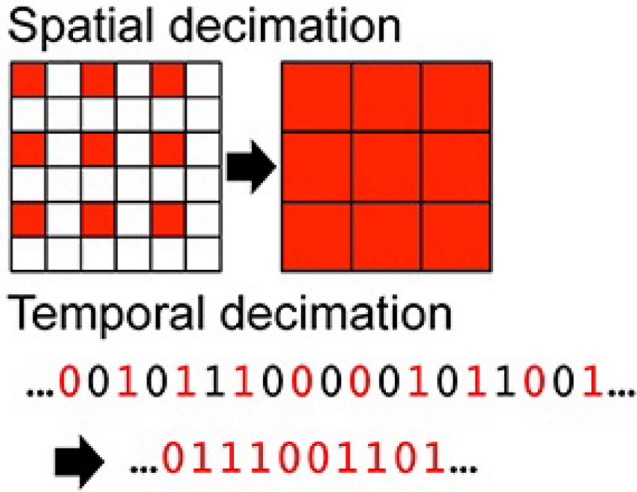


Fig. 2. Spatial and Temporal Decimation. Spatial decimation extracts the top left data point of every 2×2 grid. These extracted values are used to create the subsequent spatial scale. Temporal decimation downsamples a given time series by taking every other time point to create the next temporal scale. The example shown indicates a binary time series for an illustration purpose.

resting potential. The external current I_{ext} is the current applied to stimulate and create spiral waves. The current I_{si} is a slow inward inactivation current used to balance I_{so} and to produce the observed plateau in the action potential. The two gate variables of the model follow first order equations in time:

$$\frac{\partial u}{\partial t} = \frac{(1-p)(1-u)}{\tau_u^-} - \frac{pu}{\tau_u^+} \quad (2)$$

$$\frac{\partial w}{\partial t} = \frac{(1-p)(1-w)}{\tau_w^-} - \frac{pw}{\tau_w^+} \quad (3)$$

where

$$\tau_u^- = (1-q)\tau_{u1}^- + q\tau_{u2}^- \quad (4)$$

$$p = \begin{cases} 1 & \text{if } V \geq V_c \\ 0 & \text{if } V < V_c \end{cases} \quad (5)$$

$$q = \begin{cases} 1 & \text{if } V \geq V_u \\ 0 & \text{if } V < V_u \end{cases} \quad (6)$$

Finally, the three currents are given by the following:

$$I_{fi} = -\frac{up}{\tau_d}(V - V_c)(1 - V) \quad (7)$$

$$I_{so} = \frac{V}{\tau_0}(1 - p) + \frac{p}{\tau_r} \quad (8)$$

$$I_{si} = -\frac{w}{2\tau_{si}}(1 + \tanh(k(V - V_c^{si}))) \quad (9)$$

We chose the following model parameters to produce stable phase singularities for the study: $\tau_d = 0.395$ (msec); $\tau_u^+ = 3.33$ (msec); $\tau_{u1}^- = 9$ (msec); $\tau_{u2}^- = 8$ (msec); $\tau_0 = 9$ (msec); $\tau_r = 33.33$ (msec); $\tau_{si} = 29$ (msec); $\tau_w^+ = 250$ (msec); $\tau_w^- = 60$ (msec); $V_c = 0.13$; $V_u = 0.04$; $V_c^{si} = 0.50$; and $k = 15$.

We generated a set of a 2-D 512×512 isotropic lattice ($\Delta x = 0.025$ cm) of components by inducing spiral waves using the cross-field stimulation method [16].

2.2. Downsampling and conversion

We spatially coarse-grained the original 512×512 lattice of time

series to a 64×64 lattice by extracting the top left corner of each 8×8 block. In each component, we computed the time series of transmembrane potential for 10 s excluding the stimulation period with a time step of 0.1 msec, which was subsequently downsampled at a sampling frequency of 1000 Hz [17]. The rotors were defined as the phase singularities of the phase map as described [13]. To approximate clinical recordings, we converted the transmembrane potential derived from the model to unipolar and subsequently to bipolar electrogram (Fig. 1B) using the 64×64 lattice [18]. Briefly, conversion to the unipolar electrogram was performed by finding the sum of the Laplacian operator of the transmembrane potentials weighted by the distance around a specific component:

$$u_{i,j}(t) = \sum_{k,l=1}^{k,l=N} \frac{\nabla^2 v_{k,l}(t)}{r_{k,l}} \quad (10)$$

Here $u_{i,j}(t)$ is the unipolar signal as a node i, j , while $v_{k,l}(t)$ is the transmembrane potential at cell (k, l) . Subsequently, the bipolar electrogram was obtained by calculating the difference of unipolar potentials between two adjacent components of fixed distance.

$$w_{i,j}(t) = u_{i,j}(t) - u_{i+S,j+S}(t) \quad (11)$$

Here $w_{i,j}(t)$ is the bipolar voltage at node (i, j) , and $S = 1$, which represents our reference inter-electrode spacing.

2.3. Renormalization group

We generated a renormalization group of the system by a series of spatial and temporal coarse-graining and rescaling operations on the original microscopic description of the system (Fig. 1C) [13]. We coarse-grained the system spatially and temporally with decimation by a factor of 2. Spatial decimation transforms a $n \times n$ lattice into a $\frac{n}{2} \times \frac{n}{2}$ lattice by extracting the top left component of each 2×2 block. Temporal decimation downsampled the time series of each component by a factor of 2 (Fig. 2). Using a combination of iterative coarse-graining in spatial and temporal axes, we created a renormalization group of a total of 16 spatiotemporal scales of the system. The renormalization group included spatial scale 1 (64×64 lattice), 2 (32×32 lattice), 3 (16×16 lattice), and 4 (8×8 lattice), and temporal scales 1 (1000 Hz), 2 (500 Hz), 3 (250 Hz), and 4 (125 Hz).

2.4. Lagrangian coherent structures of information flow

We quantified the Lagrangian coherent structures (LCS) of information flow underlying the spiral waves as described previously [7]. Briefly, transfer entropy [19] is a non-parametric statistic measuring the directed reduction in uncertainty in one time-series process X (source) given another process Y (destination).

$$T_{X \rightarrow Y} = \sum p(y_{t+1}^l, y_t^l, x_t^k) \log_2 \frac{p(y_{t+1}^l | y_t^l, x_t^k)}{p(y_{t+1}^l | y_t^l)} \quad (12)$$

where k and l denote the length of time series in the processes X and Y , respectively:

$$x_t^k = (x_t, x_{t-1}, \dots, x_{t-k+1}) \quad (13)$$

$$y_t^l = (y_t, y_{t-1}, \dots, y_{t-l+1}) \quad (14)$$

$p(\alpha, \beta, \gamma)$ denotes the joint probability of the time series generated by α, β , and γ . $p(\alpha|\beta)$ denotes the conditional probability of the time series generated by α , given the time series generated by β . We adopted the standard convention $\log_2 0 = 0$.

In this study we defined k and l such that x_t^k and y_t^l contain a unit time ($= 1$ s) of the time-series preceding time t ($k = l$). By looking at the different probabilities of the 3-tuples, $(y_{t+1}^l, y_t^l, x_t^k)$, we can quantify how much better one can predict the value of y_{t+1}^l given both y_t^l and x_t^k over just y_t^l . We used the continuous transfer entropy calculator

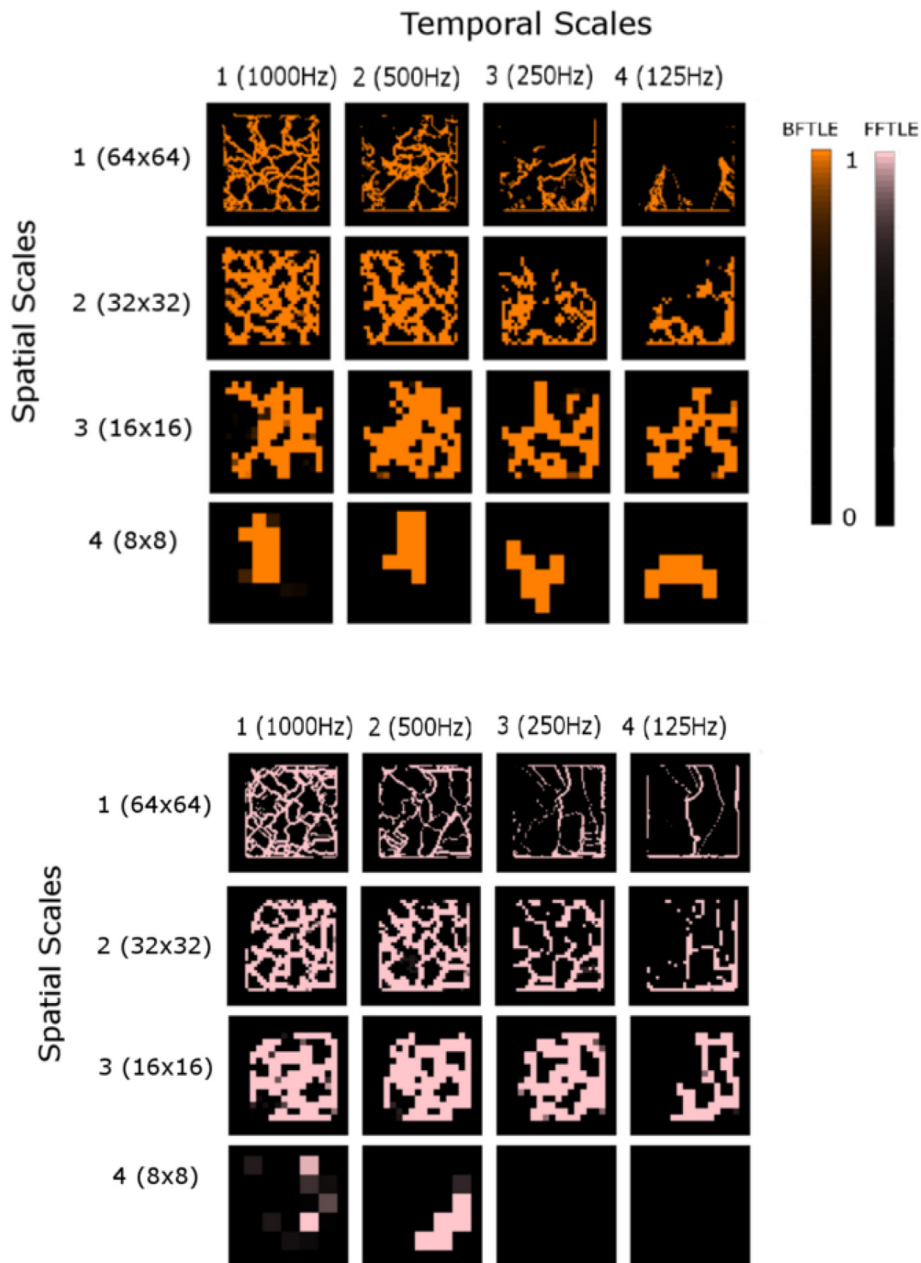


Fig. 3. Lagrangian coherent structures. The top panel (orange) shows the repelling Lagrangian coherent structures (LCS) derived from the backward finite-time Lyapunov exponents (BFTLE). The bottom panel (pink) shows the attracting LCS derived from the forward finite-time Lyapunov exponents (FFTLE). Each panel contains the renormalization group of 16 (= 4 × 4) spatiotemporal scales. For each panel, the columns represent the temporal scale (1 through 4) and the rows represent the spatial scale (1 through 4). (For interpretation of the references to color in this figure legend, the reader is referred to the Web version of this article.)

of the Java Information Dynamics Toolkit (JIDT) to calculate transfer entropy [20]. Transfer entropy was expanded to a vector field on a 2-D lattice, allowing us to define information flow as time-dependent vector fields. Then we defined an information particle as a point that moves with the local information velocity. This allowed us to compute information transport in a Lagrangian perspective. We calculated the finite-time Lyapunov exponent (FTLE) to quantify the spatially and temporally localized divergence of trajectories. The forward FTLE field was obtained by integrating the velocity forward in time from t_0 to t . Similarly, the backward FTLE field was obtained by integrating the negative velocity field backward in time from t to t_0 . The Lagrangian coherent structure (LCS) was defined as ridges, or lines of local maxima, of the FTLE field [9]. A sharp ridge is characterized by a high negative curvature, i.e., high negative eigenvalues μ of the Hessian matrix of the FTLE field $\nabla^2 \Lambda_{t_0}^t(\mathbf{x}_0)$. For points on the ridge, the gradient of the FTLE

field $\nabla \Lambda_{t_0}^t(\mathbf{x}_0)$ is tangent to the ridge line and perpendicular to the eigenvector η corresponding to the smallest eigenvalues $\mu_{\min} < 0$ of the Hessian, which leads to the condition:

$$\eta \cdot \nabla \Lambda_{t_0}^t(\mathbf{x}_0) = 0. \tag{15}$$

Repelling and attracting LCS were derived from the forward and the backward FTLE fields, respectively. The FTLE in the renormalization group was interpolated back to a 64×64 lattice using cubic spline to allow inter-scale comparison between components. The use of cubic spline to interpolate the FTLE was justified because the FTLE was derived from the cardiac electrophysiology time series, and cubic spline has been extensively used to interpolate cardiac electrophysiology time series [21].

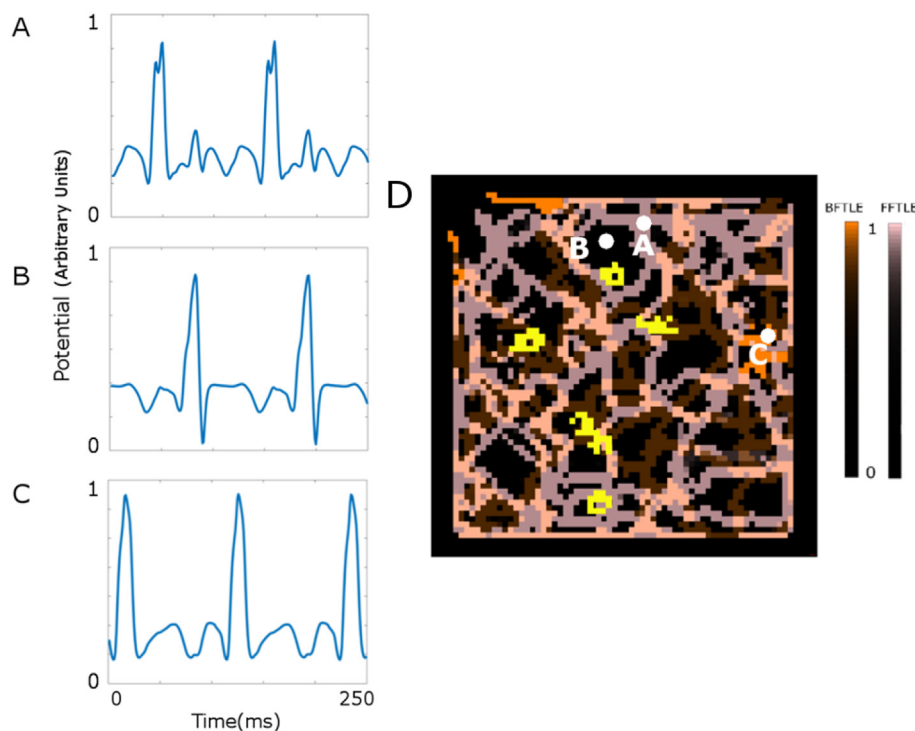


Fig. 4. Spatial relationship between bipolar electrograms, the Lagrangian coherent structures, and the rotor trajectories A, B, and C indicate the bipolar electrograms at three separate locations as marked on the Lagrangian coherent structures (D). The yellow solid lines indicate the trajectory of the phase singularities. All the data are described at the original scale (temporal scale = 1, spatial scale = 1). D. LCS A representation of the Lagrangian coherent structures (LCS) from temporal and spatial scale 1. LCS derived from the backward finite-time Lyapunov exponents (BFTLE) are shown in orange, and LCS derived from the forward finite-time Lyapunov exponents (FFTLE) are shown in pink. (For interpretation of the references to color in this figure legend, the reader is referred to the Web version of this article.)

2.5. Quantitative assessment of scale invariance of Lagrangian coherent structures

The FTLE values of each component of the lattice in each spatio-temporal scale of the renormalization group was compared with that of the original 64×64 lattice. The difference squared in value between the two corresponding components was calculated and extracted to create another 64×64 lattice that represents the FTLE error. For each component, the error was discretized to 1 when it was less than an arbitrary threshold of 0.1 or to 0 when it was equal to or greater than the threshold. The error cutoff of 0.1 was determined by the sensitivity analysis (Appendix 1, Supplementary Information).

3. Results

3.1. Lagrangian coherent structures of the renormalization group

Fig. 3 shows the repelling (top panel, orange) and the attracting LCS (bottom panel, pink) in the renormalization group. The original scale (spatial scale = 1; temporal scale = 1) shows that both the repelling (orange) and attracting LCS (pink) cover most of the lattice like a spider web. In the temporal scale 1, those web-like LCS were preserved in the spatial scales 2 and 3. However, both the repelling (orange) and attracting LCS (pink) became localized in the spatial scale 4. In the temporal scale 2, some of those LCS clearly disappeared while others were preserved. However, as in the temporal scale 1, the web-like LCS were preserved in the spatial scales 2 and 3, and lost in some regions of the spatial scale 4. In the temporal scale 3, further disappearance of LCS was observed in the spatial scales 1 and 2. However, the web-like LCS were still preserved in spatial scale 3. The attracting LCS (pink) were virtually lost in the spatial scale 4. In the temporal scale 4, LCS disappeared further but some linear structures remained in the spatial scales 1, 2 and 3. As in the temporal scale 3, the attracting LCS (pink) were lost in the spatial scale 4.

Fig. 4 shows the spatial relationship between bipolar electrograms, the Lagrangian coherent structures, and the rotor trajectories.

3.2. Scale invariance of Lagrangian coherent structures

In Fig. 5, in the temporal scale 1 (left column), preservation of the repelling LCS was observed in the spatial scales 2 and 3. However, the repelling LCS was virtually lost in the spatial scale 4 (bottom left panel). Similar observations were made in the temporal scales 2 (second left column) and 3 (second right column). In the temporal scale 4 (right column), preservation of the repelling LCS was only observed in the spatial scale 1, whereas it was virtually lost in the spatial scales 3 and 4.

For the attracting LCS (Fig. 6), preservation of LCS was observed in the spatial scales 2 and 3 of the temporal scale 1 (left column). Similar to the repelling LCS, however, the attracting LCS was virtually lost in the spatial scale 4 (bottom left panel). Similar observations were made in the temporal scales 2 (second left column) and 3 (second right column). In the temporal scale 4 (right column), preservation of the attracting LCS was only observed in the spatial scale 1, whereas it was virtually lost in the spatial scales 3 and 4. Importantly, those scale-invariant LCS were not co-localized to the trajectory of the rotors (Figs. 3 and 4).

Fig. 7 quantifies the scale invariance of the repelling (top panel) and attracting LCS (bottom panel) at each spatiotemporal scale.

4. Discussion

4.1. Main findings

Our main findings are summarized as follows. First, we found that both the repelling and attracting LCS change across the different spatial and temporal scales of the renormalization group. Second, despite the change across the scales, some LCS are scale-invariant, particularly down to the spatial and temporal scales. Third, the patterns of those scale-invariant structures are not obvious from the trajectory of the rotors based on the traditional voltage mapping of the cardiac system.

4.2. Lagrangian coherent structures of the cardiac system

The repelling LCS of information flow indicates a surface barrier that separates the individual information flow. In other words, the

Temporal Scale

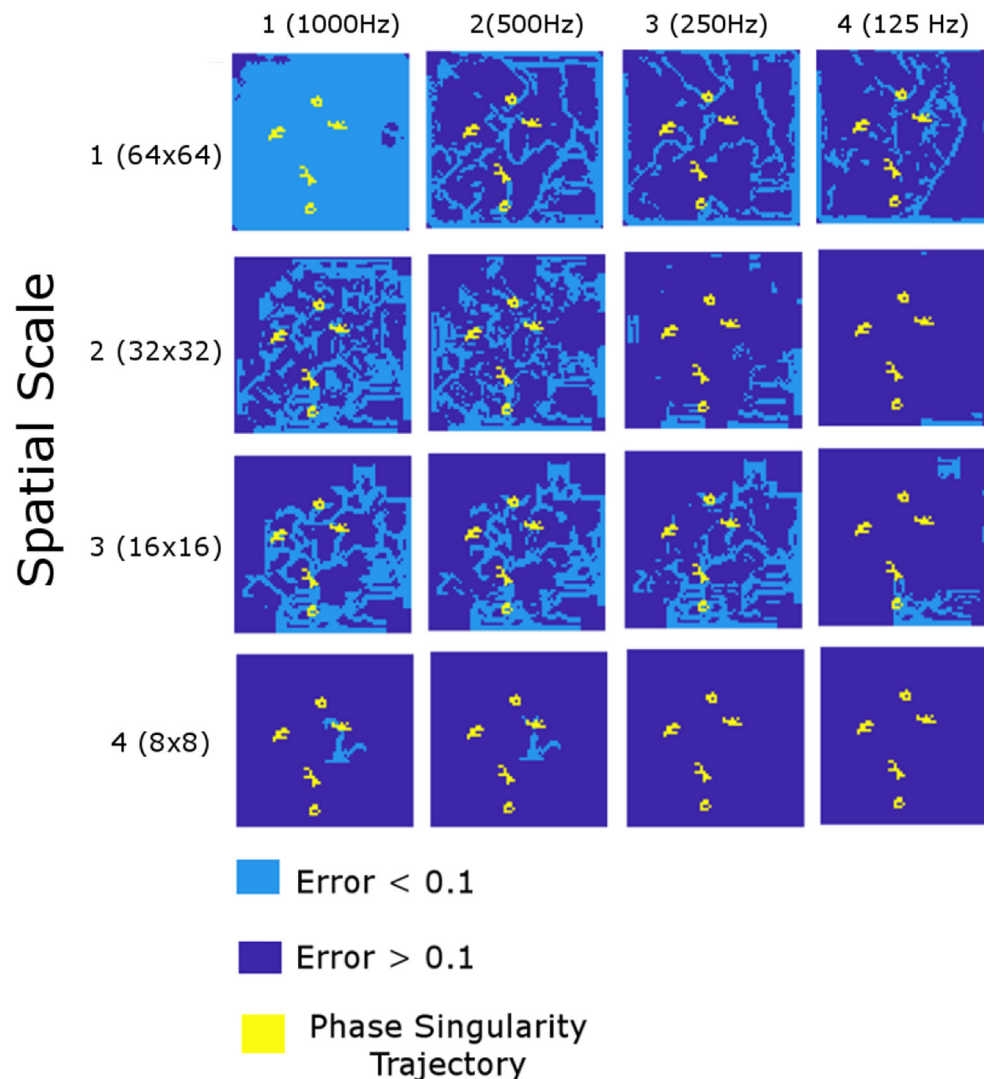


Fig. 5. Scale invariance of repelling Lagrangian coherent structures. The renormalization group of 16 ($= 4 \times 4$) spatiotemporal scales. The columns represent the temporal scale (1 through 4) and the rows represent the spatial scale (1 through 4). The components shown in light blue indicate those with the small finite-time Lyapunov exponent (FTLE) errors (< 0.1). The components shown in dark blue indicate those with the large finite-time Lyapunov exponent (FTLE) errors (≥ 0.1). The yellow solid lines represent the trajectory of the rotors. (For interpretation of the references to color in this figure legend, the reader is referred to the Web version of this article.)

repelling LCS segment the lattice into smaller segments of information dynamics. In contrast, the attracting LCS of information flow represents a region of information mixing, which can be considered as a meeting point of information particles that originate from different spiral waves. Our approach provides a tool to quantitatively characterize a macro-scale behavior of excitable media by specifically focusing on information transport, thereby quantifying the spiral wave dynamics. In our previous work, we applied LCS analysis of information flow to a simple model of excitable media to quantify the complex interactions among the components [7]. The present work extends the application of information flow LCS to multi-scale representation of a cardiac system and identification of the scale-invariant structure.

4.3. Clinical implications

Our findings have two important clinical implications. First, our analysis sheds new light on the mechanism that maintains fibrillation. Our findings indicate the presence of scale-invariant structures associated with spiral wave dynamics. The scale-invariant property of these structures quantified by the LCS indicates their possible contribution to the maintenance of spiral waves. Second, our analysis provides a new approach to quantifying fibrillation, rather than simply the presence or absence of fibrillation. Our method of quantitative analysis of human fibrillation provides patient-specific diagnostic parameters that could potentially serve as a valid endpoint for therapeutic interventions. However, the geometry of the scale-invariant LCS is not simple. Future work should focus on quantitative analyses of the scale-invariant LCS to determine how it could contribute to maintenance of spiral waves.

Temporal Scale

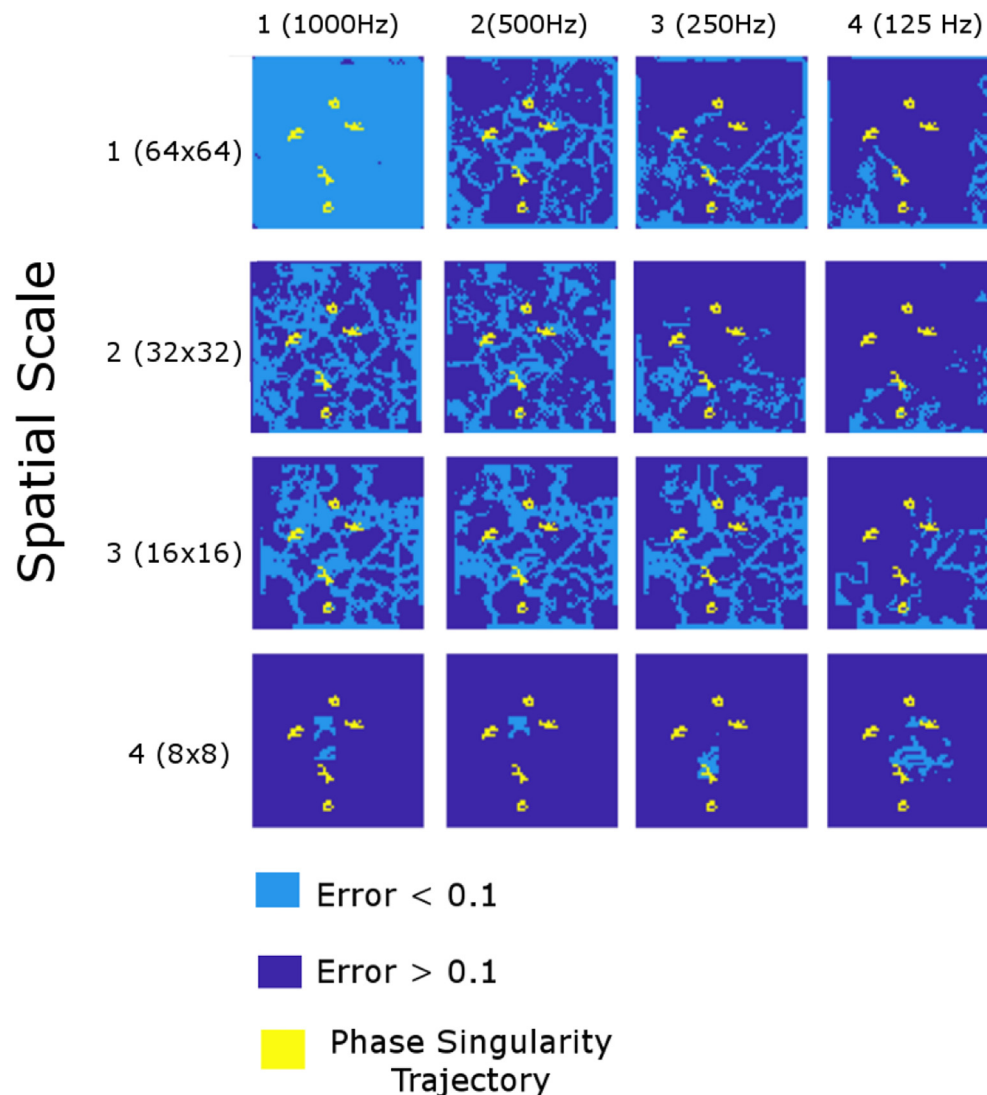


Fig. 6. Scale invariance of attracting Lagrangian coherent structures. The renormalization group of 16 ($= 4 \times 4$) spatiotemporal scales. The columns represent the temporal scale (1 through 4) and the rows represent the spatial scale (1 through 4). The components shown in light blue indicate those with the small finite-time Lyapunov exponent (FTLE) errors (< 0.1). The components shown in dark blue indicate those with the large finite-time Lyapunov exponent (FTLE) errors (≥ 0.1). The yellow lines represent the trajectory of the rotors. (For interpretation of the references to color in this figure legend, the reader is referred to the Web version of this article.)

4.4. Limitations

We recognize several limitations associated with the numerical method we implemented. We used the Fenton-Karma model, which is a relatively simple cardiac model, with a homogeneous and isotropic 2-D lattice. It is possible that a more biophysically detailed model of the heart with anatomical heterogeneity, anisotropy and a more realistic geometry could make our approach more difficult to analyze; however, the information-theoretic approach that we used in the study was independent of the underlying ionic model specifications. In addition, the simplicity of the cardiac model is an advantage that allows the results from this model to be widely applicable to other reaction-diffusion systems. The LCS in this work are the organizing manifolds of information flow. Unstable and/or multiple wavelets can still define the LCS as long as the manifolds can be defined in a given period of time. If

the rotors are too unstable to create manifolds, the LCS cannot be defined.

5. Conclusions

The Lagrangian coherent structures of information flow underlying spiral waves are preserved across multiple spatiotemporal scales. A multi-scale approach to the information flow within the cardiac system provides a quantitative tool to improve our understanding of the mechanism of fibrillation.

Acknowledgements

The research reported in this publication was supported by the National Heart Lung and Blood Institute of the National Institutes of Health.

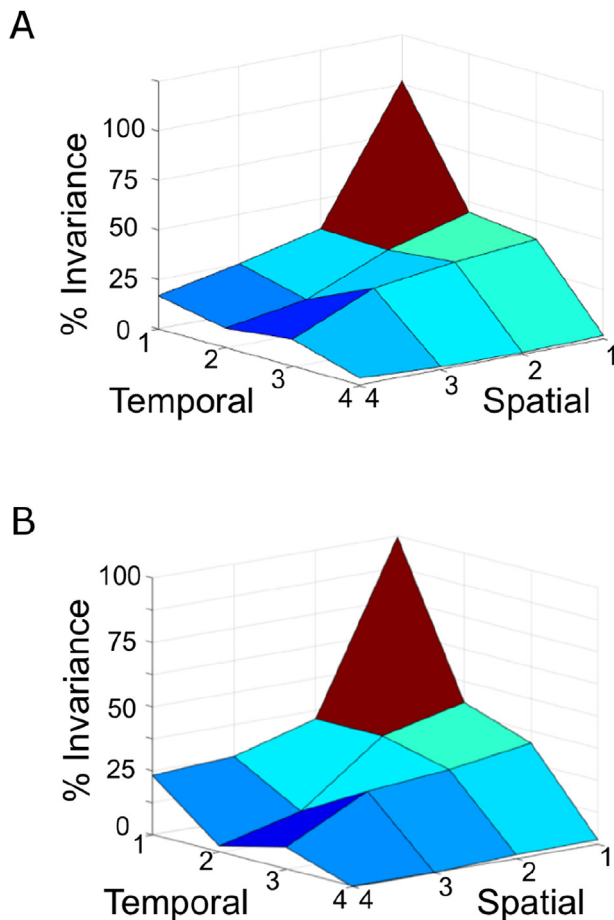


Fig. 7. Quantitative assessment of scale invariance. The x-axis is the spatial scale [scale 1 (64×64 lattice), scale 2 (32×32 lattice), scale 3 (16×16 lattice), and scale 4 (8×8 lattice)]. The y-axis is the temporal scale [scale 1 (1000 Hz), scale 2 (500 Hz), scale 3 (250 Hz), and scale 4 (125 Hz)]. The z-axis is % invariance, indicating the fraction of components on the lattice at each spatio-temporal scale with the error of the finite-time Lyapunov exponent (FTLE) less than 0.1. A. *Repelling LCS*, B. *Attracting LCS*.

Health under Award No. T32HL007227 (to K.N.A.). The percentage of the total program project costs financed with Federal money is 100%. The content is solely the responsibility of the authors and does not necessarily represent the official views of the National Institutes of Health. This research was also supported by the Fondation Leducq Transatlantic Network of Excellence 16CVD02 (to H.A.).

Appendix A. Supplementary data

Supplementary data to this article can be found online at <https://doi.org/10.1016/j.compbiomed.2018.11.005>.

Conflicts of interest

Daniel Sohn None declared.
Konstantinos N. Aronis None declared.
Hiroshi Ashikaga None declared.

References

- [1] G.Y.H. Lip, L. Fauchier, S.B. Freedman, I. Van Gelder, A. Natale, C. Gianni, S. Nattel, T. Potpara, M. Rienstra, H.-F. Tse, D.A. Lane, Atrial fibrillation, *Nat. Rev. Dis. Primers* 2 (2016) 16016 <https://doi.org/10.1038/nrdp.2016.16>.
- [2] M. Haissaguerre, M. Hocini, A. Denis, A.J. Shah, Y. Komatsu, S. Yamashita, M. Daly, S. Amraoui, S. Zellerhoff, M.-Q. Picat, et al., Driver domains in persistent atrial fibrillation, *Circulation* 130 (7) (2014) 530–538.
- [3] P. Benharash, E. Buch, P. Frank, M. Share, R. Tung, K. Shivkumar, R. Mandapati, Quantitative analysis of localized sources identified by focal impulse and rotor modulation mapping in atrial fibrillation, *Circ. Arrhythm. Electrophysiol.* 8 (3) (2015) 554–561.
- [4] C. Gianni, S. Mohanty, L. Di Biase, T. Metz, C. Trivedi, Y. Gökoğlan, M.F. Güneş, R. Bai, A. Al-Ahmad, J.D. Burkhardt, et al., Acute and early outcomes of focal impulse and rotor modulation (firm)-guided rotors-only ablation in patients with nonparoxysmal atrial fibrillation, *Heart Rhythm* 13 (4) (2016) 830–835.
- [5] R.F. Berntsen, T.F. Håland, R. Skårdal, T. Holm, Focal impulse and rotor modulation as a stand-alone procedure for the treatment of paroxysmal atrial fibrillation: a within-patient controlled study with implanted cardiac monitoring, *Heart Rhythm* 13 (9) (2016) 1768–1774.
- [6] E. Buch, M. Share, R. Tung, P. Benharash, P. Sharma, J. Koneru, R. Mandapati, K.A. Ellenbogen, K. Shivkumar, Long-term clinical outcomes of focal impulse and rotor modulation for treatment of atrial fibrillation: a multicenter experience, *Heart Rhythm* 13 (3) (2016) 636–641.
- [7] H. Ashikaga, R.G. James, Hidden structures of information transport underlying spiral wave dynamics, *Chaos* 27 (1) (2017) 013106.
- [8] G. Haller, G. Yuan, Lagrangian coherent structures and mixing in two-dimensional turbulence, *Phys. Nonlinear Phenom.* 147 (3–4) (2000) 352–370.
- [9] S.C. Shadden, F. Lekien, J.E. Marsden, Definition and properties of Lagrangian coherent structures from finite-time Lyapunov exponents in two-dimensional aperiodic flows, *Physica D* 212 (3) (2005) 271–304.
- [10] G. Haller, Lagrangian coherent structures, *Annu. Rev. Fluid Mech.* 47 (2015) 137–162.
- [11] H. Ashikaga, R.G. James, Inter-scale information flow as a surrogate for downward causation that maintains spiral waves, *Chaos: Interdiscip. J. Nonlinear Sci.* 28 (7) (2018) 075306.
- [12] L.P. Kadanoff, Scaling laws for Ising models near T_c , *Physics* 2 (6) (1966) 263–272.
- [13] H. Ashikaga, F. Prieto Castrillo, M. Kawakatsu, N. Dehghani, Causal scale of rotors in a cardiac system, *Front. Physiol.* 6 (2018) 30.
- [14] F. Fenton, A. Karma, Vortex dynamics in three-dimensional continuous myocardium with fiber rotation: filament instability and fibrillation, *Chaos: Interdiscip. J. Nonlinear Sci.* 8 (1) (1998) 20–47.
- [15] F.H. Fenton, E.M. Cherry, H.M. Hastings, S.J. Evans, Multiple mechanisms of spiral wave breakup in a model of cardiac electrical activity, *Chaos* 12 (3) (2002) 852–892.
- [16] A.M. Pertsov, J.M. Davidenko, R. Salomonsz, W.T. Baxter, J. Jalife, Spiral waves of excitation underlie reentrant activity in isolated cardiac muscle, *Circ. Res.* 72 (3) (1993) 631–650.
- [17] H. Ashikaga, A. Asgari-Targhi, Locating order-disorder phase transition in a cardiac system, *Sci. Rep.* 8 (1) (2018) 1967.
- [18] K.N. Aronis, H. Ashikaga, Impact of number of co-existing rotors and inter-electrode distance on accuracy of rotor localization, *J. Electrocardiol.* 51 (2018) 82–91.
- [19] T. Schreiber, Measuring information transfer, *Phys. Rev. Lett.* 85 (2) (2000) 461.
- [20] J.T. Lizier, Jid: an information-theoretic toolkit for studying the dynamics of complex systems, *Front. Robot. AI* 1 (2014) 11.
- [21] E. Cicaccio, Dynamic relationship of cycle length to reentrant circuit geometry and to the slow conduction zone during ventricular tachycardia, *Circulation* 103 (2001) 1017–1024.